JOINT EUROPEAN TORUS

JET–P(93)74

J. Egedal, H. Bindslev

Topology of Relativistic Refractive Index Surfaces for Electron Cyclotron Waves

Topology of Relativistic Refractive Index Surfaces for Electron Cyclotron Waves

J. Egedal, H. Bindslev

JET-Joint Undertaking, Culham Science Centre, OX14 3DB, Abingdon, UK

Preprint of a paper to be submitted for publication in
Plasma Physics and Controlled Fusion
September 1993

ABSTRACT

The dispersion of electron cyclotron waves in a relativistic Maxwellian plasma is investigated. It is shown that the apparently very complicated picture of the coupling of the extraordinary (X) mode to Bernstein waves can be accounted for in a simple way by considering the refractive indices as Riemann–like surfaces in the Clemmow–Mullaly–Allis (CMA) parameter space, $({\omega_p}^2/\omega^2, \omega_c/\omega)$, and by introducing a few topological concepts from the analysis of complex functions. A detailed study is made of the surface representing the X mode for perpendicular propagation, with special attention given to the connection between this mode and Gross–Bernstein modes. For perpendicular propagation non–transcendental approximations to the relativistic refractive indices for X and O modes can be given. We show that these approximations are good up to $\sim$ 25 keV and that at frequencies up to the second harmonic of the electron cyclotron frequency the X mode approximation also accounts correctly for the connection of the X mode to Bernstein modes. The accuracy and the numerical efficiency of the approximations make them well suited for routine calculations for millimetre wave applications in fusion plasmas, including the analysis of X mode and O mode reflectometry.

1 INTRODUCTION

The dispersion of plasma electron cyclotron waves has been investigated by many authors including BORNATICI et al. (1981) (1983), ROBINSON (1986a) (1987a,b) (1988), LAZZARO and RAMPONI (1981) and BATCHELOR et al. (1984). Significant relativistic effects in both the real and the imaginary parts of the refractive index have been found even when the mean thermal energy of the plasma electrons is small compared to the rest mass energy of an electron.

It has been demonstrated that these relativistic modifications are of practical consequence to a number of microwave experiments on magnetically confined fusion plasmas. In particular it has been found that in millimeter wave Thomson scattering [BINDSLEV, 1991a] and in reflectometry [BINDSLEV, 1991b and 1992] it may be essential to take relativistic effects into account when analyzing results. Also, diagnostics relying on electron cyclotron emission can be affected by the relativistic increase in the cutoff density [COSTLEY and BARTLETT, 1993].

The need to take relativistic dielectric effects into account in a range of applications, including those mentioned above, adds to the desirability of having a detailed knowledge of the dispersion of waves in a relativistic plasma under a wide range of parameters, and to have accurate relativistic expressions which may be evaluated with a minimum of computing time.

In this paper we show that the apparently very complicated picture of the connection of the extraordinary (X) mode with Bernstein waves [LAZZARO and RAMPONI, 1981;

BORNATICI et al. 1981; ROBINSON, 1986a and 1988] can be accounted for in a simple way by introducing a few topological concepts from the analysis of complex functions. We consider each refractive index as a sheet in the Clemmow–Mullaly–Allis (CMA) parameter space, $(\omega_p^2/\omega^2, \omega_c/\omega)$, and find that these sheets are connected to form one continuous Riemann-like surface.

One of the general difficulties in studying relativistic effects on the dispersion of waves is that the dispersion function is a transcendental function of the refractive index, and thus a root search is required for each evaluation of the index.

For the study of the X mode surface at frequencies lower than the second harmonic a simplified dispersion function can be used [ROBINSON 1986a], which includes finite Larmor radius effects only to first order in $(k_\perp \rho)^2$, where ρ is the mean electron Larmor radius. This approximation is good for the X mode, and accounts accurately for the coupling to Bernstein modes for frequencies up to the second harmonic of the electron cyclotron frequency. The advantage of the approximation is that it permits the refractive index to be given as an explicit function of the plasma parameters and thus provides an efficient and accurate routine for use, for example, in density profile reconstruction from X mode reflectometry.

The paper is organized as follows. In Section 2 we discuss the general characteristics of electron cyclotron wave dispersion and the connection between the X mode and Bernstein modes. It is shown that in the vicinity of degenerate roots the refractive index considered as a surface in the CMA space generally has a structure similar to that of a two-sheeted Riemann surface near a branch point. As an example we investigate in Section 3 the sheet corresponding to the X mode near a point, where it coincides with a sheet corresponding to a Bernstein wave. In Section 4 we analyse in detail the dispersion along a specific trajectory through the CMA parameter space in order to expose the main features of the dispersion of the X mode and the associated Bernstein mode in the region of the R cutoff and the upper hybrid resonance for $\omega_c < \omega < 2\omega_c$. In previous studies the refractive index was often plotted as a function of frequency, with all other parameters constant. In Section 5 analyses of this kind are put into four categories corresponding to the positions of the trajectories in the CMA diagram relative to the positions of the branch points. Connections between Gross–Bernstein modes and the extraordinary mode near the upper hybrid resonance are discussed in Section 6. The temperature dependence of the refractive index is considered in Section 7. Relativistic effects on the dispersion of the O mode are discussed briefly in Section 8, and a non-transcendental approximation to the O mode refractive index is given. Finally, in Section 9 the approximation for the X mode refractive index, introduced in Section 3, is discussed in detail.

2 GENERAL CHARACTERISTICS OF ELECTRON CYCLOTRON WAVE DISPERSION

In the electron cyclotron frequency range the ion dynamics can be ignored and the dispersion function, $D = |\varepsilon + N^2(\widehat{\mathbf{k}}\widehat{\mathbf{k}} - \mathbf{I})|$, is a function of T_e, B, n_e, ω, θ and N, where T_e is the electron temperature, B is the magnetic field, n_e is the electron density, ω is the angular frequency, θ is the angle between the magnetic field, $\mathbf{B}$, and the wave–vector, $\mathbf{k}$, and $N = kc/\omega$ is the refractive index. Here we consider D as a function of the independent variable set (X, Y, T_e, θ, N), where $X = (\omega_p/\omega)^2$ and $Y = \omega_c/\omega$ are the CMA parameters, while $\omega_p = \sqrt{n_e q_e^2/(m_e \varepsilon_0)}$ is the electron plasma frequency, and $\omega_c = |q_e|B/m_e$ is the electron cyclotron frequency.

For a given set of values of (X, Y, T_e, θ) the weakly relativistic dispersion relation, $D = 0$, has an infinite number of solutions in N, each of which are in general continuous functions of (X, Y, T_e, θ). In the subsequent analysis we will generally keep T_e and θ fixed and consider the solutions for N as sheets in the CMA plane (X, Y).

Two roots in the dispersion relation may coincide at a point, (X_0, Y_0). Under certain conditions the sheets involved have the same topology in the neighbourhood of the degenerate point, (X_0, Y_0), as a two–sheeted Riemann surface near a branch point. This phenomenon will be referred to as *connection* between the sheets, and the associated points will be referred to as *branch points*.

Assume that the dispersion relation has a double root, N_0, at the point $\mathbf{b_0} = (X_0, Y_0)$, and that D is analytic at this point. This implies that

$$D(N_0, \mathbf{b_0}) = 0 \quad ,$$

$$\frac{\partial D(N_0, \mathbf{b_0})}{\partial N} = 0$$

and

$$\frac{\partial^2 D(N_0, \mathbf{b_0})}{\partial N^2} \neq 0 \quad .$$

To obtain the structure of the solution–planes in the neighbourhood of the double root, we expanded D around $\mathbf{b_0}$:

$$D(N_0 + \delta N, \mathbf{b_0} + \boldsymbol{\delta}) = (\delta N)^2 \frac{1}{2} \frac{\partial^2 D(N_0, \mathbf{b_0})}{\partial N^2} + \delta X \frac{\partial D(N_0, \mathbf{b_0})}{\partial X} + \delta Y \frac{\partial D(N_0, \mathbf{b_0})}{\partial Y} \quad , \tag{1}$$

where $(\mathbf{b_0} + \boldsymbol{\delta}) = (X_0 + \delta X,\ Y_0 + \delta Y)$. Solving for δN in the dispersion relation, $D(N_0 + \delta N, \mathbf{b_0} + \boldsymbol{\delta}) = 0$, gives

$$\delta N = \sqrt{\frac{\delta X \frac{\partial D(N_0, \mathbf{b_0})}{\partial X} + \delta Y \frac{\partial D(N_0, \mathbf{b_0})}{\partial Y}}{\frac{1}{2} \frac{\partial^2 D(N_0, \mathbf{b_0})}{\partial N^2}}} \quad . \tag{2}$$

From expression (2) and provided

$$Im \left\{ \left(\frac{\partial D(N_0, \mathbf{b_0})}{\partial X} \right)^* \frac{\partial D(N_0, \mathbf{b_0})}{\partial Y} \right\} \neq 0 \tag{3}$$

it follows that the refractive index surface near the degenerate point has the same structure as a two–sheeted Riemann surface near a branch point.

3 BRANCH POINTS AND CONNECTION IN THE X MODE SURFACE

The contour plot in Figure 1 is obtained with the weakly relativistic model given by SHKAROFSKY (1986) which is based on an expansion of the dielectric tensor, $\boldsymbol{\varepsilon}$, in powers of $\lambda_e = (k_\perp \rho_e)^2$, where $\rho_e = (T_e/(\omega_c{}^2 m_e))^{\frac{1}{2}}$ is the mean thermal Larmor radius of the electrons. The plot shows the real part of N in the CMA plane for the X mode with $(T_e,\ \theta)$ = (15.0 keV, 90^0). $\theta = 90^0$ implies that there is no Doppler broadening of the resonances, but only broadening due to the relativistic increase of the mass of the electrons. For comparison Figure 2 shows a contour plot of the X mode refractive index predicted by cold theory.

In Figure 2 the R cutoff is the straight line from (1,0) to (0,1) corresponding to the zero level. In Figure 1 the R cutoff is almost straight, but here it goes from (1.07,0) to (0.07,1). Figures 1 and 2 also show small parts of the L cutoff, the same shift being found here. These shifts in the cutoffs are due to relativistic effects and are discussed in detail in BORNATICI and RUFFINA (1988) and BINDSLEV (1993). Note that for low densities (here for $X < 0.07$) there is no true cutoff.

In the plot for the cold X mode the upper hybrid resonance is seen clearly as the parabolic curve $1 = X + Y^2$ along which the refractive index is infinite. In Figure 1 the refractive index does not go to infinity at the upper hybrid frequency; instead we observe a ridge along which N has a finite value. The location of the ridge almost coincides with the location of the resonance curve predicted by the cold theory, but the ridge ends above the second harmonic of the electron cyclotron frequency $(1 > Y > 1/2)$.

Anomalous dispersion [SHKAROFSKY, 1966], which is absent in the cold theory, is clearly visible in Figure 1 at the lower harmonics of ω_c.

The discontinuities in Figure 1 are not physically significant, but are simply a consequence of the fact that the plot only shows one of the solutions to the dispersion relation. This solution in fact joins continuously to other solution at the discontinuities shown here. In this plot one discontinuity is placed between the two branch points, $\mathbf{b_2}$ and $\mathbf{b_3}$, while the other is placed between the branch point, $\mathbf{b_1}$, and a point on the edge of the CMA plane. Because of the similarity between these discontinuities and the branch cuts in complex function theory, we will refer to the discontinuities as ***branch cuts***.

BORNATICI et al. (1981), LAZZARO and RAMPONI (1981) and ROBINSON (1986a) investigated the dispersion of the X mode between the first and second harmonic of ω_c for perpendicular propagation by considering approximations to the refractive index of the form:

$$N^2 = \frac{-B \pm \sqrt{B^2 - 4AC}}{2A} \quad , \tag{4}$$

where A, B and C are functions of $(X,\ Y,\ T_e)$ but independent of N. When referring to (4) we will have in mind the expression given by ROBINSON (1986a), since this is the most general. It accounts accurately for the connection between the X mode and Bernstein modes for frequencies up to the second harmonic of ω_c. For convenience we include in the Appendix expressions for A, B and C.

From expression (4) we find that the cutoff conditions for both the R and L cutoffs are given by $C = 0$, which is identical to the weakly relativistic cutoff condition [BINDSLEV, 1993]. Degenerate solutions are found where $\Delta = B^2 - 4AC = 0$. Figure 3 shows curves in the CMA plane where $C = 0$, $Re(\Delta) = 0$ and $Im(\Delta) = 0$ respectively: we see that there are three points, $\mathbf{p_1}$, $\mathbf{p_2}$ and $\mathbf{p_3}$, where the condition, $\Delta = 0$, is satisfied. These points are branch points in the approximation (4) and correspond to the three branch points, $\mathbf{b_1}$, $\mathbf{b_2}$ and $\mathbf{b_3}$, obtained with the weakly relativistic dispersion relation. Note that the branch point $\mathbf{b_1}$ is found on the high density side of the high field limit of the R cutoff, while both $\mathbf{b_2}$ and $\mathbf{b_3}$ are on the low density side of the cutoff.

The existence of the points $\mathbf{b_2}$ and $\mathbf{b_3}$ was first indicated by LAZZARO and RAMPONI (1981) and BORNATICI et al. (1981), but the two–sheeted Riemann structure in the vicinity of these points was not pointed out.

The plots in Figure 4 demonstrate this structure of the refractive index surface in the neighbourhood of $\mathbf{b_3}$. Figure 4(a) shows a contour plot of a sheet which contains a part of the R cutoff and which may be identified as the sheet corresponding to the X mode. The contour plot in Figure 4(b) covers the same parameter space as the plot in Figure 4(a) but here the sheet corresponds to a Gross–Bernstein wave. The branch cuts in the two plots are placed identically and the plots may be connected along these cuts. A dashed curve is drawn in each of the plots. These two curves join each other at the points marked s_1 and s_2 and may be considered as a single closed curve which circulates twice around the branch point. The refractive index can be followed continuously on this curve. Starting at the point s_0 with the value N_0 for the refractive index and letting the CMA parameters follow the curve, one finds that after one circulation round the branch point the refractive index is not equal to N_0 even though we return to the point s_0. However, after two circulations round the branch point the refractive index does return to the original value N_0. This illustrates that the refractive index has the structure of a two-sheeted Riemann surface.

For Y higher than a specific limit, Y_l, ($Y_l > 1/2$) the resonance condition corresponding to the second harmonic of ω_c will only be satisfied in the very warm tail of the electron distribution. In the interval $Y_l < Y < 1$ we thus find that $Im(\Delta) \simeq 0$. We will refer to the two dashed curve sections in Figure 3 for which $Re(\Delta) = 0$ and $Y_l < Y < 1$ as d and e, where d is the curve nearest to the R cutoff. From expression (4) we find that on the curves d and e the two values of N^2 under consideration (N_+^2 and N_-^2) are very close. The distance between them gets smaller as Y approaches unity, but $N_+^2 \neq N_-^2$ until $Y = 1.00$ where the branch point $\mathbf{b_1}$ is located.

The sign of the damping rate is always positive in an isotropic Maxwellian plasma ($Im(N) \geq 0$), so when calculating N from N^2 a square root with the branch cut just below the positive real axis must be used. It then turns out that the two sheets associated with N_+ and N_- are almost touching each other on d ($N_+ \simeq N_-$), while on e we find that $N_+ \simeq -N_-$. The location of curve section e in Figure 3 coincides with the location of the ridge in Figure 1 while the position of curve section d is identical with the position of the upper edge of the shelf in Figure 1.

4 QUALITATIVE FEATURES OF THE X MODE DISPERSION

In order to expose the interaction between the X mode and the relevant Bernstein mode for $Y > 1/2$, we now discuss the most important features of the dispersion curves found by plotting the refractive indices as functions of Y with $X/Y^2 = 0.8$. The intersection between the curves $X/Y^2 = 0.8$ and $Re(\Delta) = 0$ is close to the second harmonic of ω_c which makes the effect of the imaginary part in Δ more visible. We will refer to the mode going to the R cutoff as N_- and the mode going to the L cutoff as N_+.

The plots in Figure 5 show respectively the values of $Re(N_\pm)$ and $Im(N_\pm)$ obtained with the relativistic dispersion relation [SHKAROFSKY, 1986] by following the trajectory $X/Y^2 = 0.8$ for $0.50 < Y < 0.90$. The values of Y where $C = 0$, and $Re(\Delta) = 0$ are called Y_c, Y_d and Y_e respectively (corresponding to Figure 3), and are marked on the plots. The main features of these dispersion curves may be listed as follows:

- On the low field side of the R cutoff ($Y < Y_c$) it is found that $Re(N_\pm) > 0$ and $Im(N_\pm) > 0$. Here N_+ corresponds to a heavily damped mode, while N_- corresponds to the mode known as the X mode.
- At the cutoff (Y_c) we find as expected, that N_- is zero, while the other mode is

unaffected.

- On the high field side of the cutoff we find that $Re(N_-) < 0$ and $Im(N_-) > 0$. Since N_- must be damped we conclude that the group velocity and the phase velocity of this mode are in opposite directions. After the cutoff both modes are heavily damped.

- As Y approaches Y_d the difference between N_+ and N_- becomes very small, but the imaginary part of Δ keeps the two curves apart. $Im(\Delta)$ in fact keeps the two sheets associated with N_+ and N_- apart along d all the way up to the branch point, $\mathbf{p_1}$.

- For $Y < Y_d$ we have $Re(\Delta) > 0$, but for $Y_d < Y < Y_e$ we find that $Re(\Delta) < 0$. Because of this, and the fact that $|Re(\Delta)| \gg |Im(\Delta)|$, the square root of Δ in (4) suddenly adds a large imaginary part to N_+^2 and N_-^2. None of the other terms in (4) seem to add a significant imaginary part, so for Y between Y_d and Y_e we find that $N_+ \simeq -N_-^*$.

- At the point Y_e the imaginary parts of both N_+ and N_- are small, and we see a maximum in N_+. The peak in N_+ is what is left of the upper hybrid resonance after the relativistic broadening of the cyclotron resonances. Since $Re(\Delta) = 0$ and $Im(\Delta) \simeq 0$ we have, from (4), that $N_-^2 \simeq N_+^2$, which here corresponds to $N_- \simeq -N_+$.

- For $Y > Y_e$ we have $Re(\Delta) > 0$ so the imaginary parts of $N_\pm$ are again small. We still find that $Re(N_-) < 0$ and $Im(N_-) \simeq 0$, and consequently that N_- is a negligibly damped mode for which the group velocity and the phase velocity are in opposite directions. N_+ is the mode going to L cutoff, and is also lightly damped.

In the WKB approximation considered here coupling does not exist at points where the sheets do not coincide mathematically. The only interaction between modes in this model is the connection found as a consequence of branch points. However, on the curves d and e, where we have that $N_+^2 \simeq N_-^2$, a full wave solution may show that there is coupling between the two modes. ROBINSON (1986a) appears to suggest that this coupling should be similar to the connection corresponding to the two branch points $\mathbf{b_2}$ and $\mathbf{b_3}$ at the second harmonic of the cyclotron resonance, but from the analysis given here we find that these phenomena are not identical.

5 CATEGORISATION OF PREVIOUS STUDIES

The connection of the X mode to Bernstein modes at the first and second harmonic of the cyclotron frequency is often investigated by plotting the refractive indices as functions of the frequency, ω, for constant temperature, T_e, and for a fixed ratio between the density and the magnetic field, n_e/B. This corresponds to obtaining the refractive index as functions of $1/Y$ for different values of T_e and X/Y^2. We repeat this here but choose to plot the dispersion curves as functions of $Y \propto 1/\omega$ instead of $1/Y$. The topologies of these curves depend on the positions of the trajectories in the CMA diagram relative to the positions of the branch points. The trajectories ($X/Y^2 = constant$) are put into the following categories, in each of which the behaviour of the refractive index is different.

1. Curves passing on the low density side of all three branch points;
2. Curves passing through the R cutoff and between branch points 1. and 2;
3. Curves passing through the R cutoff and between branch points 2. and 3;
4. Curves passing through the R cutoff and on the high density side of all three branch points.

Figure 6 shows trajectories in the CMA plane corresponding to the different categories.

1. Category 1 can be sub–divided into two further categories:
   (a) Curves passing on the low density side of the cutoff and all of three branch points.
   (b) Curves passing through the cutoff and on the low density side of all three branch points.

   Curves of this kind were analyzed by BORNATICI and RUFFINA (1988) and ROBINSON (1986a, 1987b).

   Figure 7 shows plots of $Re(N)$ corresponding respectively to categories 1(a) and 1(b). In the area of the CMA plane where these plots are obtained $\lambda_e > 1$ for the Bernstein wave, so the plots of this mode are only qualitative. The difference between the two categories is simply due to the fact that in category 1(a) the curves $X/Y^2 = constant$ pass on the low density side of the R cutoff and therefore $Re(N_x^2) > 0$ everywhere, while this is not the case in category 1(b). Here an interval appears where $Re(N_x^2) < 0$, and at the first point where $Re(N_x^2) = 0$ we find the cutoff. This does not give rise to any topological difference between the two cases.

2. In category 2 the curves $X/Y^2 = constant$ pass on the high density side of $\mathbf{b_1}$. This causes a topological change relative to category 1, as may be seen by comparing Figure 7 with Figure 8. For the solution in N which goes to the cutoff we see that the real part now remains negative after the cutoff, and the solution which previously represented the Bernstein mode now takes over the role of being the X mode at the high field end. Dispersion in this category has been analyzed by BORNATICI and RUFFINA (1988) and ROBINSON (1986a, 1987b). The case analyzed above, where we followed the trajectory $X/Y^2 = 0.8$, is in this category. By comparing Figure 8 with Figure 5(a) it can be seen how the relativistic broadening of the cyclotron resonances smooths out the sharp edges in the refractive index for increasing temperature.

3. In category 3 the two branch points $\mathbf{b_1}$ and $\mathbf{b_2}$ are passed on the high density side. Category 3 is similar to category 1, because here it is once again the same branch which represents the X mode at both the low and the high field ends. However, the mode which at the low and high field ends represents a Bernstein mode goes down to the R cutoff as seen in Figure 9, but this does not represent a topological difference between category 3 and category 1. An earlier investigation of dispersion in this category was made by BORNATICI (1981), and similar curves were obtained by LAZZARO and RAMPONI (1981).

4. Categories 2 and 4 are similar to each other in the same way that categories 1 and 3 are. This is due to the fact that branch points $\mathbf{b_1}$, $\mathbf{b_2}$ and $\mathbf{b_3}$ all connect the same two sheets. The topology of the two curves that result from following a two–sheeted Riemann–like surface along a certain trajectory depends only on the parity of the number of branch points on either side of the trajectory. Trajectories in categories 1 and 3 pass an even number of branch points on the high field side, while trajectories in categories 2 and 4 pass an odd number. The only significant difference between the plot given in Figure 10 and that in Figure 8 is that the shelf just after the cutoff in Figure 8 has disappeared in Figure 10, this being due to relativistic broadening of the cyclotron resonances.

6 CONNECTION BETWEEN THE X MODE AND GROSS–BERNSTEIN MODES NEAR THE UPPER HYBRID RESONANCE

In Figure 1 a finite ridge, limited to the range $1/2 < Y < 1$, is found near the location of the cold upper hybrid resonance. On the low density side of this ridge the existence of a strong absorption band was demonstrated in Figure 5. In a limited frequency range just above $2\omega_c$ this absorption band vanishes.

The plots in Figure 11 show $Re(N)$ and $Im(N)$ as functions of X with $Y = 0.495$ for the two solutions to the weakly relativistic dispersion relation, which go to the R and to the L cutoffs respectively. The imaginary part of the mode, which goes to the L cutoff, is seen to be very small, and no sign of the upper hybrid resonance is seen in either the real part or in the imaginary part. The latter mode which in the low density end corresponds to a Gross–Bernstein mode diverges for $X \simeq 0.32$ and cannot be followed by the weakly relativistic dispersion function used here. In a Tokamak it may be possible to obtain similar parameter variations as the one used in Figure 11 by launching a wave straight down from the top of the plasma. The presence of absorption layers at the electron cyclotron frequency and its harmonics makes it difficult to access the region between the upper hybrid resonance and the L cutoff with X mode for $\omega > \omega_c$. However, mode conversion between the two modes shown in Figure 11 would make it possible to reach this region without encountering significant absorption. This may be of interest for Electron Cyclotron Resonance Heating.

Figure 12 shows a new contour plot of the refractive index. The difference between this plot and that given in Figure 1 is that the branch cuts have been placed in different locations. By comparing Figure 2 and Figure 12 it can be seen that for $Y > 1$ the cold theory is in good agreement with the weakly relativistic model, except for the anomalous dispersion at the cyclotron resonances and the downshift in frequency due to the relativistic increase of the electron mass. In considering the mode going to the L cutoff, for $Y < 1$ we can still find some agreement between the cold and the relativistic theory. The plot in Figure 12 shows that finite ridges, such as the one found for $1/2 < Y < 1$, exist between all the harmonics of ω_c, at least for frequencies up to the 5th harmonic. In the analysis above we found that the curve section e in Figure 3 shows the location of the ridge for $1/2 < Y < 1$, and it was found that here the two solutions considered satisfied $N_- \simeq N_+$. For frequencies between other harmonics, up to the 5th and probably higher, the case is similar. Here we again find solutions, N, with the group velocities and phase velocities in opposite directions, and which at the location of the ridges fulfill $N \simeq -N_{ridge}$.

The areas in Figure 12 with dotted background show where $Im(N) > 0.01$. For frequencies slightly above a harmonic of the electron cyclotron frequency, and densities higher than a certain limit, the modes are almost undamped. Dispersion curves similar to those shown in Figures 11(a) and 11(b) can consequently be obtained for frequencies slightly higher than each harmonic at least up to the 5th harmonic.

For frequencies higher than the 5th harmonic we find that $\lambda_e > 1$, which means that the convergence of the dispersion function [SHKAROFSKY, 1986] used for calculation of the plot is not guaranteed. Certain reservations must therefore be made for the region in Figure 12 where $0 < Y < 0.2$.

For frequencies between the sth and $(s+1)$th harmonic the sheets corresponding to the sth and $(s+1)$th lightly damped classical Gross–Bernstein modes are connected [ROBINSON, 1988]. We have found that these connections also are associated with branch points and two–sheeted Riemann structures. These branch points are located on the low density side of the upper hybrid resonance for $Y < 1/2$. On the high density side of the branch points the Gross–Bernstein modes form one continuous mode which goes to the L cutoff. Cuts corresponding to the branch points are present in Figure 12, but they are masked by the high density of contour lines. They extend horizontally from the branch points to the branch cut between the edge of the CMA plane and $\mathbf{b_3}$. Note that a surface corresponding to the sth classical Gross–Bernstein mode is not limited to frequencies near the sth harmonic of the electron cyclotron frequency, but in general we find that the mode is heavily damped for other frequencies.

For lower densities additional branch points occur in the Gross–Bernstein sheets (these sheets are not shown in this region in Figure 12). Because of the strong damping in this region we will not investigate the dispersion for these branches in any further detail.

The main features of the dispersion for the Gross–Bernstein modes near the upper hybrid resonance can be summarized as follows:

- Finite ridges similar that found between the first and second harmonics of the electron cyclotron frequency also exist between higher harmonics.

- At each of the ridges another solution, N, exists which satisfies $N \simeq -N_{ridge}$, and for which the group and phase velocity are in opposite directions.
- For frequencies just above a harmonic and up to the frequency found at the relevant ridges the two above mentioned modes, N and N_{ridge}, are almost undamped.
- For densities below the cold upper hybrid resonance branch points occur. Here the sheets corresponding to the classical Gross–Bernstein modes are connected and form the lightly damped mode which goes to the L cutoff.
- As the density approaches zero the Gross–Bernstein modes diverge. This can be explained by the fact that they do not exist in vacuum.

The above results indicate a pattern in which the dispersion described near the location of the cold upper hybrid for $\omega_c < \omega < 2\omega_c$ is repeated for frequencies between higher harmonics.

7 THE TEMPERATURE DEPENDENCE OF THE X MODE REFRACTIVE INDEX

The contour plots in the text above were all obtained with $T_e = 15$ keV. The main features in these plots do not, however, change qualitatively with temperature.

By using the asymptotic expressions for the Dnestrovskii functions, F_q, it may be shown that as the temperature goes to zero the distance between the curve sections d and e in Figure 3 vanishes as well, and in the cold limit the two curve sections coincide and form the upper hybrid resonance ($1 = X + Y^2$) for frequencies below the second harmonic ($1/2 < Y < 1$).

The downshift in the cutoff frequencies, due to the relativistic increase of the electron mass, vanishes as the temperature approaches zero.

The absorption bands in the CMA diagram gather just above each harmonic of the electron cyclotron frequency as the temperature decreases. The positions of the branch points also change with temperature. Approximations for the locations of the three branch points $\mathbf{b}_1$, $\mathbf{b}_2$ and $\mathbf{b}_3$ may be given as follows.

$$\begin{aligned}
X_{\mathrm{b1}} &\simeq 5.608\cdot 10^{-3}\left(\frac{T_{e0}}{\mathrm{keV}}\right) - 8.02\cdot 10^{-5}\left(\frac{T_{e0}}{\mathrm{keV}}\right)^2 \quad , \\
Y_{\mathrm{b1}} &\simeq 1.000 \quad , \\
\\
X_{\mathrm{b2}} &\simeq 0.2837 + 4.00\cdot 10^{-4}\left(\frac{T_{e0}}{\mathrm{keV}}\right) + 3.42\cdot 10^{-5}\left(\frac{T_{e0}}{\mathrm{keV}}\right)^2 \quad , \\
Y_{\mathrm{b2}} &\simeq 0.5000 + 3.20\cdot 10^{-3}\left(\frac{T_{e0}}{\mathrm{keV}}\right) - 1.73\cdot 10^{-5}\left(\frac{T_{e0}}{\mathrm{keV}}\right)^2 \quad , \\
\\
X_{\mathrm{b3}} &\simeq 0.4960 - 3.20\cdot 10^{-3}\left(\frac{T_{e0}}{\mathrm{keV}}\right) + 5.11\cdot 10^{-5}\left(\frac{T_{e0}}{\mathrm{keV}}\right)^2 \quad , \\
Y_{\mathrm{b3}} &\simeq 0.5000 + 8.00\cdot 10^{-3}\left(\frac{T_{e0}}{\mathrm{keV}}\right) - 6.84\cdot 10^{-5}\left(\frac{T_{e0}}{\mathrm{keV}}\right)^2 \quad .
\end{aligned} \tag{5}$$

If $\mathbf{b_2}$ and $\mathbf{b_3}$ were to coincide they would neutralize each other so it is interesting to see that the distance between $\mathbf{b_2}$ and $\mathbf{b_3}$ in the CMA diagram is almost constant, even down to the cold limit.

The surface for the refractive index predicted by the cold theory for perpendicular propagation may be obtained from the weakly relativistic dispersion relation by placing branch cuts as straight lines, between $\mathbf{b_2}$ and $\mathbf{b_3}$ and from $\mathbf{b_1}$ down to the edge of the CMA plane via the location of the upper hybrid resonance, and then letting the temperature approach zero. However, the topologies of the surfaces obtained with the weakly relativistic dispersion relation and the cold theory respectively will not be identical, because of the connection to Bernstein waves, for instance between $\mathbf{b_2}$ and $\mathbf{b_3}$, which persists in the low temperature limit.

The representations given here for the refractive index may be generalized by obtaining the positions of the branch points and absorption layers for other angles of propagation relative to $\mathbf{B}$. Note that the position of the cutoff does not depend on the angle. In LAZZARO and RAMPONI (1981) the movement of $\mathbf{b_2}$ as a function of $N_{\parallel}$ is considered. It was found that X_{b2} has a strong dependence on $N_{\parallel}$, which causes $\mathbf{b_2}$ to move out to the R cutoff for propagation at oblique angles. LAZZARO and RAMPONI (1981) also gave an approximation for Y_{b2} which was a linear function of T_{e0}. Their approximation has the wrong sign for the dependence of T_{e0} but is otherwise in agreement with the first order form of the expression for Y_{b2} given above.

8 THE DISPERSION OF THE O MODE

The dispersion of the O mode for propagation perpendicular to the magnetic field is quite simple compared with the dispersion of the X mode. For the ordinary mode no connections to the Bernstein modes are found on the low density side of the O mode cutoff, so relativistic effects on ordinary Bernstein waves [ROBINSON 1987a] will not be considered in the present work.

The main correction to the refractive index for the O mode resulting from inclusion of relativistic effects is the increase of the cutoff density, and the anomalous dispersion found for frequencies just below harmonics of the electron cyclotron frequency.

In BINDSLEV (1992) a simple approximation to the real part of the refractive index for the O mode was given. The expression was obtained for perpendicular propagation by using the cold model modified by a temperature dependent increase in the electron mass, calculated such that the cutoff coincides with the relativistic cutoff. This approximation holds good for temperatures up to ~ 25 keV and for all frequencies away from the first few harmonics of the electron cyclotron frequency.

Another approximation for the index, which accounts accurately for the anomalous dispersion at the first and second harmonics, may be derived for propagation perpendicular to the magnetic field. By solving the reduced weakly relativistic dispersion relation for the O mode, $0 = \Gamma_{33} - N^2$, we find

$$N_O^2 = \frac{1 - P_1 \pm \sqrt{(P_1 - 1)^2 - 4P_2P_0}}{2P_2} \quad . \tag{6}$$

Here Γ_{33}, P_0, P_1 and P_2 are given in the Appendix. Note that the solution, (−), corresponds to the cold O mode, when the branch cut of the square root is placed along the negative real axis (and assuming $\sqrt{1} = 1$).

Contributions to the real part of the refractive index corresponding to anomalous dispersion at higher harmonics than the second are negligible, and thus the approximation (6) is in general accurate to three or more significant digits.

9 VALIDITY OF THE APPROXIMATION FOR THE X MODE REFRACTIVE INDEX

To give an impression of the quality of the approximation (4), a contour plot of the precision in per cent, i.e. $|(Re(N_x) - Re(N_{ap}))/Re(N_x)| * 100\%$, is shown in Figure 13. Here N_x is the solution to the weakly relativistic dispersion relation for the extraordinary mode, while N_{ap} is the value of the approximation (4) corresponding to N_x. The branch cuts in Figure 13 are placed identically to the branch cuts in Figure 1, so Figure 1 shows $Re(N_x)$ used for the calculation of Figure 13. In Figure 13 it is seen that the approximation is accurate for most of the CMA plane. At the third harmonic of the cyclotron frequency the maximum error is 2–3%. This deviation is due to the anomalous dispersion, which as previously mentioned is not included in the approximation for the the third or higher harmonics of ω_c. Near the two branch points $\mathbf{b_2}$ and $\mathbf{b_3}$ the largest deviation between $Re(N_x)$ and $Re(N_{ap})$ is found to be 10%. Deviations of this kind are only seen in a limited area near the second harmonic. It is found that the indication given here for the precision of the approximation is typical for any temperature in the interval $0 < T_e < 25$ keV, which is the temperature interval in which the weakly relativistic approximation is good.

When using the approximation (4) it is important to make a careful choice of the branch cut for the square root, since this defines the locations of branch cuts for the approximation in the CMA plane. Figure 14 shows a contour plot of $Arg(\Delta)$. A specific curve in Figure 14 corresponding to a level, A, shows the location of the branch cuts for the approximation when the branch cut for the square root is placed at the angle A in the complex plane. Figure 14 shows that if the branch cut for the square root is placed along the positive imaginary axis (90^0) then one branch cut in the approximation will go through the L cutoff passing on the high field side of the electron cyclotron resonance from $\mathbf{b}_1$, while the other branch cut connects $\mathbf{b}_2$ and $\mathbf{b}_3$ along an almost straight line.

10 CONCLUSION

We have investigated the dispersion of electron cyclotron waves in a weakly relativistic Maxwellian plasma. By considering the refractive indices as surfaces in the CMA parameter space we have shown that in the vicinity of a degenerate root the sheets involved are in general connected and in such a region the structure of the surface is similar to that of a two-sheeted Riemann surface near a branch point. The dispersion of X mode and associated Bernstein modes is discussed in detail for perpendicular propagation. The main features of the dispersion are illustrated with contour plots of the principal sheets of the corresponding refractive index surface. Furthermore we find that the topology of dispersion curves evaluated along various trajectories in the CMA plane is determined by the locations of the trajectories relative to the locations of the branch points. Approximations for the locations of the three branch points, $\mathbf{b}_1$, $\mathbf{b}_2$ and $\mathbf{b}_3$, are given as functions of temperature. For perpendicular propagation non-transcendental approximations can be derived for the O and X mode refractive indices by accounting for finite Larmor radius effects only to first order in λ_e. We have shown that these expressions hold good for the O and X modes and thus provide efficient and accurate routines for use e.g. in reflectometry.

REFERENCES

BATCHELOR D. B., GOLDFINGER R. C.and WEITZNER H. (1984) *Phys. Fluids,* **27**, 2835.

BINDSLEV H. (1991a) *Plasma Physics and Controlled Fusion,* **33**, 1775.

BINDSLEV H. (1991b) Proceedings of the International School of Plasma Physics "Piero Caldirola", p. 779, Varenna.

BINDSLEV H. (1992) *Plasma Physics and Controlled Fusion,* **34**, 1601.

BINDSLEV H. (1993) *Plasma Physics and Controlled Fusion,* **35**, 1093.

BORNATICI M., ENGELMANN F., MAROLI C. and PETRILLO V. (1981) *Plasma Physics,* **23**, 89.

BORNATICI M., CANO R., DE BARBIERI O. and Engelmann F. (1983) *Nuclear Fusion,* **23**, 1153.

BORNATICI M. and RUFFINA U. (1988) *Plasma Physics and Controlled Fusion,* **30**, 113.

COSTLEY A. C. and BARTLETT D. V. (1993) Proceedings of the 8th Joint Workshop on ECE and ECRH (EC8), IPP III/186 Vol. 1, p. 159, Garching.

LAZZARO E. and RAMPONI G. (1981) *J. Plasma Physics,* **23**, 53.

ROBINSON P. A. (1986a) *J. Plasma Physics,* **35**, 187.

ROBINSON P. A. (1986b) *J. Math. Phys.,* **27**, 1206.

ROBINSON P. A. (1987a) *J. Plasma Physics,* **37**, 435.

ROBINSON P. A. (1987b) *J. Plasma Physics,* **37**, 449.

ROBINSON P. A. (1988) *Phys. Fluids,* **31**, 107.

SHKAROFSKY I. P. (1966) *J. Phys. Fluids,* **9**, 516.

SHKAROFSKY I. P. (1986) *J. Plasma Physics,* **35**, 319.

APPENDIX: THE REDUCED WEAKLY RELATIVISTIC DISPERSION RELATION

Γ_{ij} is the dielectric tensor that results when only terms to first order in λ_e are included for perpendicular propagation,

$$\Gamma_{ij} = \begin{bmatrix} S_0 + S_1 N^2 & -i(D_0 + D_1 N^2) & 0 \\ i(D_0 + D_1 N^2) & T_0 + T_1 N^2 & 0 \\ 0 & 0 & P_0 + P_1 N^2 + P_2 N^4 \end{bmatrix} \quad . \qquad \text{(A.1)}$$

Here

$$S_0 = 1 - \frac{K_1}{2}\left(F_{\frac{5}{2}}(\phi_1) + F_{\frac{5}{2}}(\phi_{-1})\right) \quad ,$$

$$S_1 = -\frac{K_1 K_2}{2}\left(F_{\frac{7}{2}}(\phi_2) + F_{\frac{7}{2}}(\phi_{-2}) - F_{\frac{7}{2}}(\phi_1) - F_{\frac{7}{2}}(\phi_{-1})\right) \quad ,$$

$$T_0 = S_0 \quad ,$$

$$T_1 = -\frac{K_1 K_2}{2}\left(F_{\frac{7}{2}}(\phi_2) + F_{\frac{7}{2}}(\phi_{-2}) - 3F_{\frac{7}{2}}(\phi_1) - 3F_{\frac{7}{2}}(\phi_{-1}) + 4F_{\frac{7}{2}}(\phi_0)\right) \quad ,$$

$$D_0 = -\frac{K_1}{2}\left(-F_{\frac{5}{2}}(\phi_1) + F_{\frac{5}{2}}(\phi_{-1})\right) \quad ,$$

$$D_1 = -\frac{K_1 K_2}{2}\left(-F_{\frac{7}{2}}(\phi_2) + F_{\frac{7}{2}}(\phi_{-2}) + 2F_{\frac{7}{2}}(\phi_1) - 2F_{\frac{7}{2}}(\phi_{-1})\right) \quad ,$$

$$P_0 = 1 - K_1 F_{\frac{5}{2}}(\phi_0) \quad ,$$

$$P_1 = -\frac{K_1 K_2}{2}\left(F_{\frac{7}{2}}(\phi_1) + F_{\frac{7}{2}}(\phi_{-1}) - 2F_{\frac{7}{2}}(\phi_0)\right) \quad ,$$

$$P_2 = -\frac{K_1 K_2^2}{8}\left(F_{\frac{9}{2}}(\phi_2) + F_{\frac{9}{2}}(\phi_{-2}) - 4F_{\frac{9}{2}}(\phi_1) - 4F_{\frac{9}{2}}(\phi_{-1}) + 6F_{\frac{9}{2}}(\phi_0)\right) \quad ,$$

$$K_1 = \mu_e X \quad , \qquad K_2 = \frac{1}{\mu_e Y^2} \quad .$$

$$F_q(\phi_m) = -i\int_0^\infty (1 - it)^{-q} \exp\left[-i\phi_m^2 t\right] dt \quad , \quad \phi_m^2 = -\mu_e(1 - mY) \quad .$$

The dispersion relations for the O and X modes for perpendicular propagation are given respectively by

$$0 = \varepsilon_{33} - N_O^2 \quad , \tag{A.2}$$

$$0 = \varepsilon_{11}(\varepsilon_{22} - N_X^2) - \varepsilon_{12}\varepsilon_{21} \quad . \tag{A.3}$$

By using Γ_{ij} rather than ε_{ij} the dispersion relations become biquadratic equations in N:

$$0 = P_2 N_O^4 + (P_1 - 1) N_O^2 + P_0 \quad , \tag{A.4}$$

$$0 = A N_X^4 + B N_X^2 + C \quad , \tag{A.5}$$

where

$$A = S_1(T_1 - 1) - D_1^2 \quad , \quad B = S_1 T_0 + S_0(T_1 - 1) - 2 D_0 D_1 \quad , \quad C = S_0 T_0 - D_0^2$$

From (A.4) and (A.5) we thus obtain the explicit expressions, (4) and (6), for N^2.

Evaluation of the Dnestrovskii functions, F_q, is readily carried out by using its series expansion or its continued fraction representation [ROBINSON, 1986b; see also correction given in BINDSLEV, 1993].

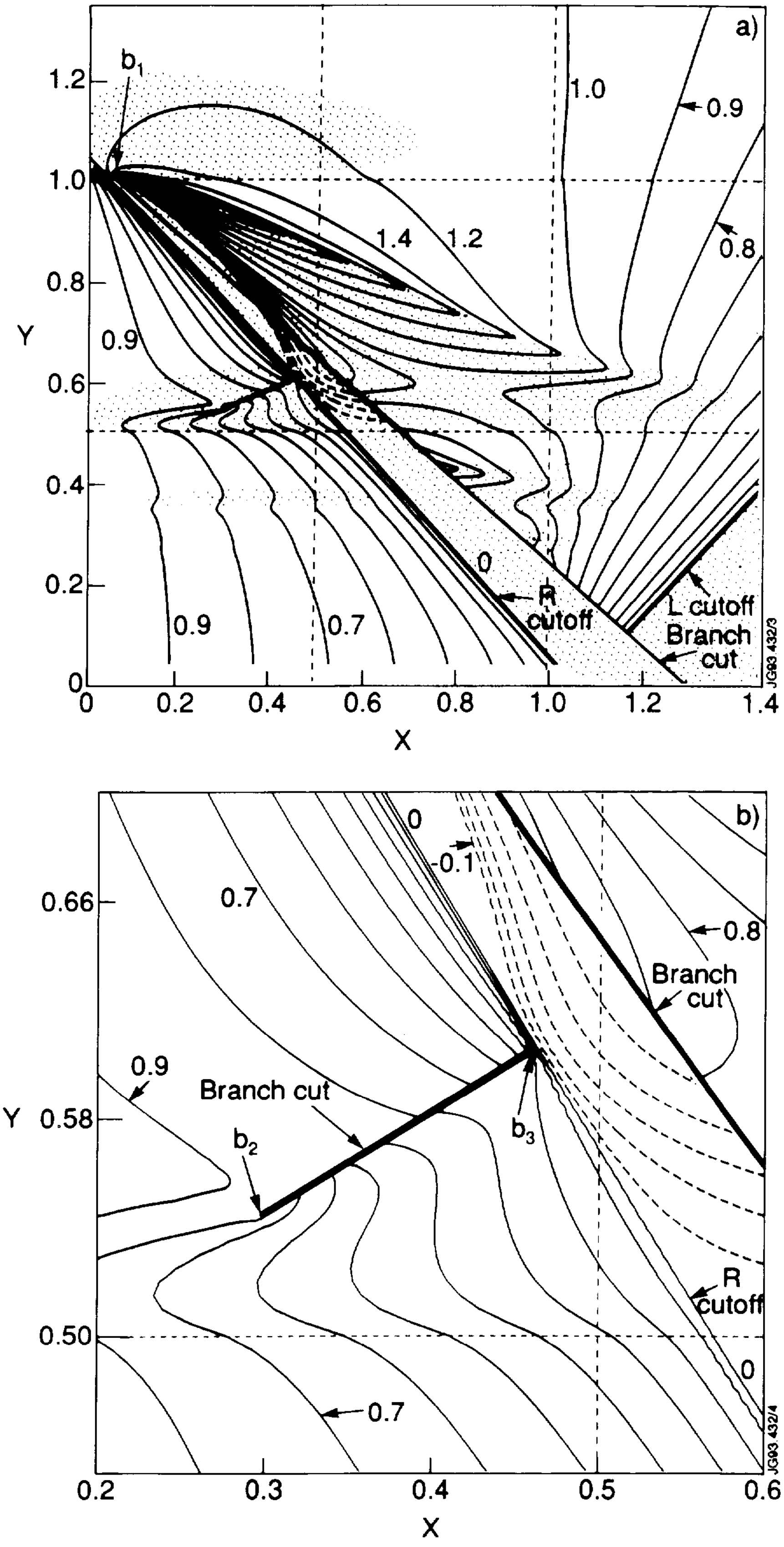

Figure 1: Contour plots of the real part of the refractive index, $Re(N)$, in the CMA parameter space. The plots are obtained with the weakly relativistic model [SHKAROFSKY, 1986] for propagation perpendicular to the magnetic field for T_e=15 keV. The steps between the contour levels are 0.1 for $-1 < Re(N) < 1$ and 0.2 for $1 < Re(N)$. For $Re(N) < 0$ the contour lines are broken. In plot (a) regions with significant damping, $Im(N) > 0.01$, are marked by a dotted background. Because of the Riemann structure in the surface two branch cuts have been laid into the plots. Plot (b) shows the region around branch points $\mathbf{b_2}$ and $\mathbf{b_3}$ in greater detail.

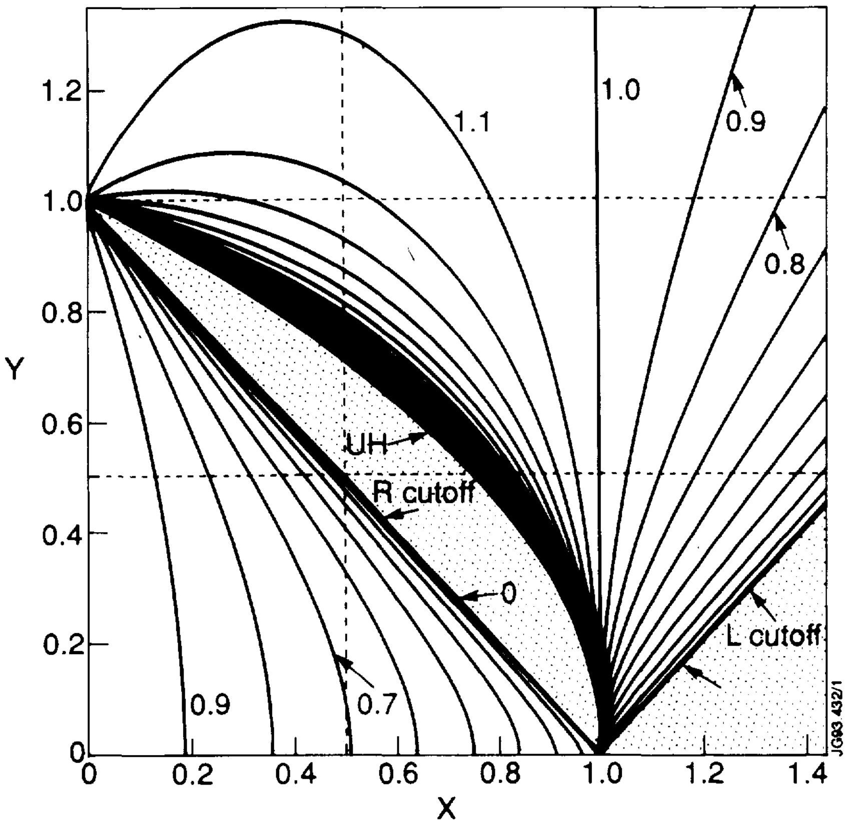

Figure 2: Contour plot of the refractive index obtained with the cold model. The distance between the contour levels is 0.1. An imaginary part in the refractive index only appears when $Re(N) = 0$ and is here marked by a dotted background.

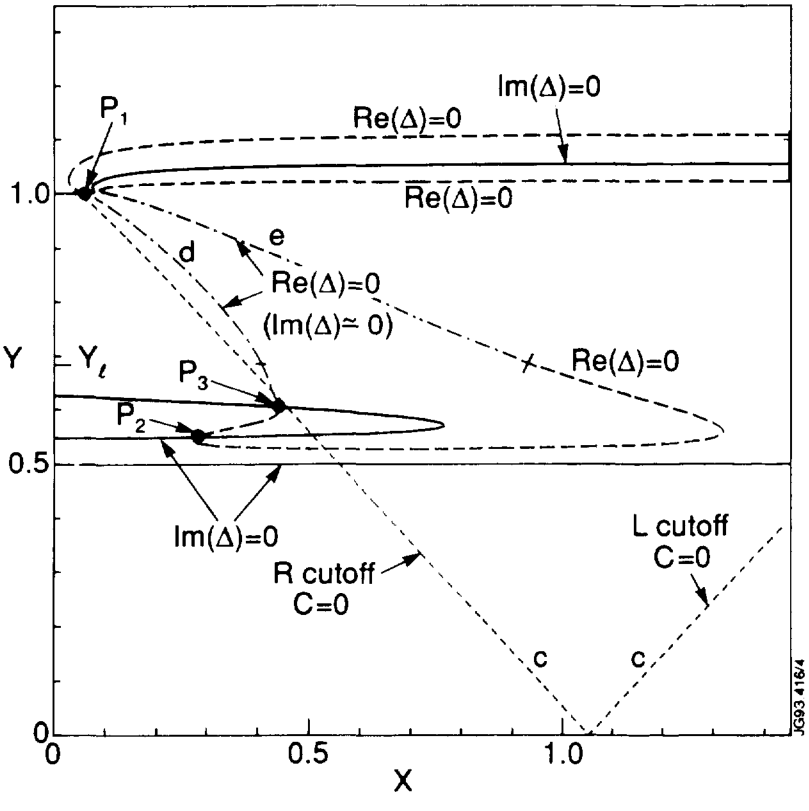

Figure 3: Zero curves for C, $Re(\Delta)$ and $Im(\Delta)$ in the CMA diagram with T_e=15 keV. The following signatures are used for the curves $C = 0$ (- - - -), $Re(\Delta) = 0$ (— —), $Re(\Delta) = 0$ and $Im(\Delta) \simeq 0$ (— - — -), $Im(\Delta) = 0$ (——). The three points where $\Delta = 0$ correspond to the three branch points $\mathbf{p}_1$, $\mathbf{p}_2$ and $\mathbf{p}_3$ in the approximation.

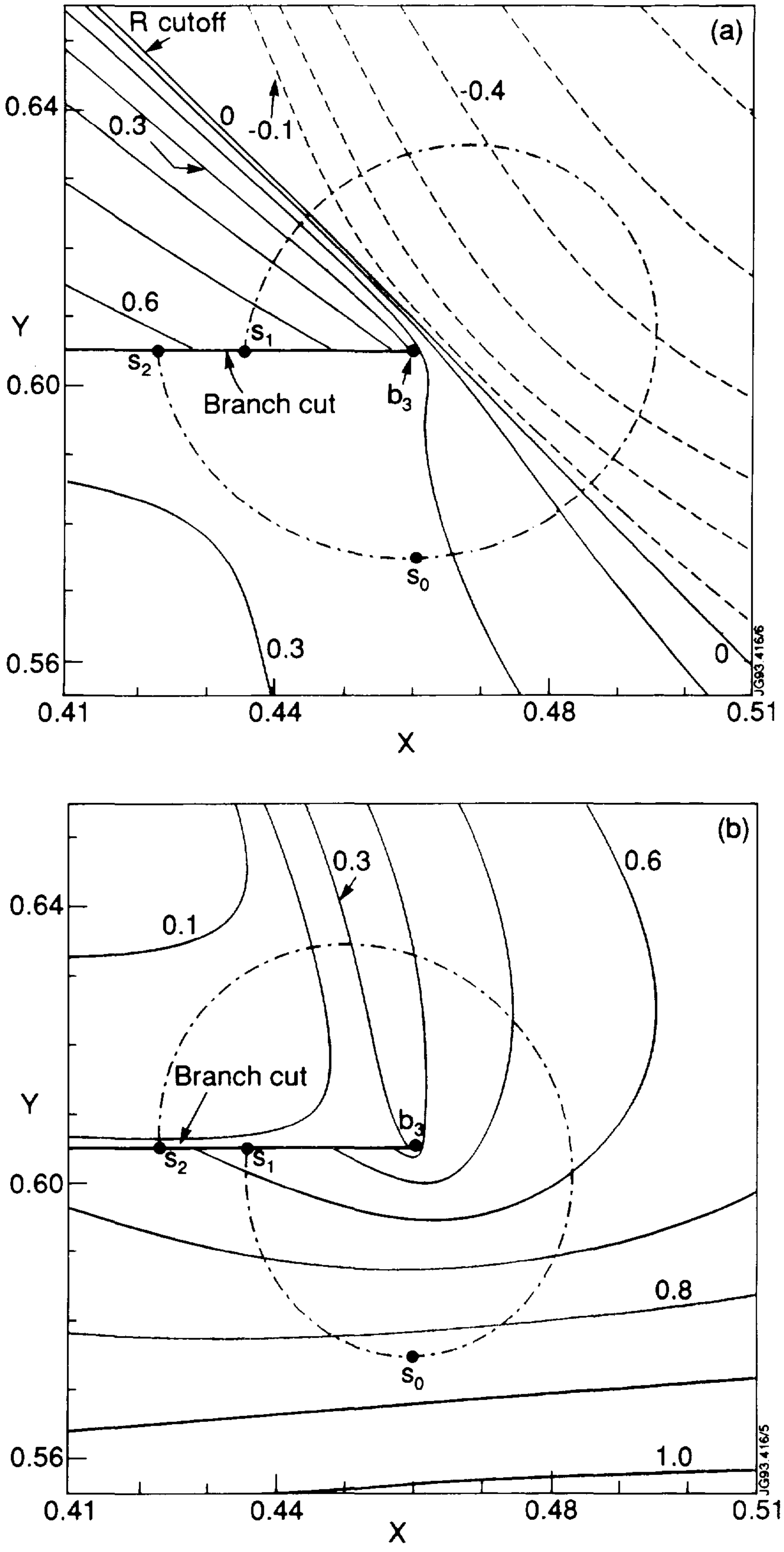

Figure 4: Contour plots of the real part of the refractive index, $Re(N)$, for a part of the double sheeted surface around a branch point. The sheet shown in (a) contains a part of the R cutoff, and may be connected along the branch cut to the sheet shown in (b). The plots are obtained by the weakly relativistic model with ($\theta = 90^0$, T_e=15 keV). The step between the contour levels is 0.1. For $Re(N) < 0$ the contour lines are broken. The refractive index varies continuously along the dashed line, returning to its original value only after two circulations of the branch point.

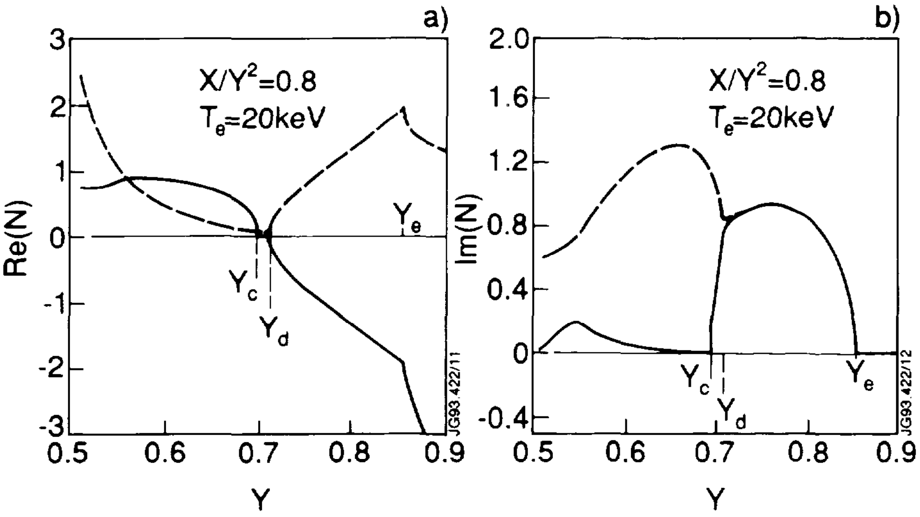

Figure 5: The refractive index along $X^2/Y = 0.8$ as a function of Y with $T_e = 20$ keV. The plots show: (a) $Re(N)$ and (b) $Im(N)$.

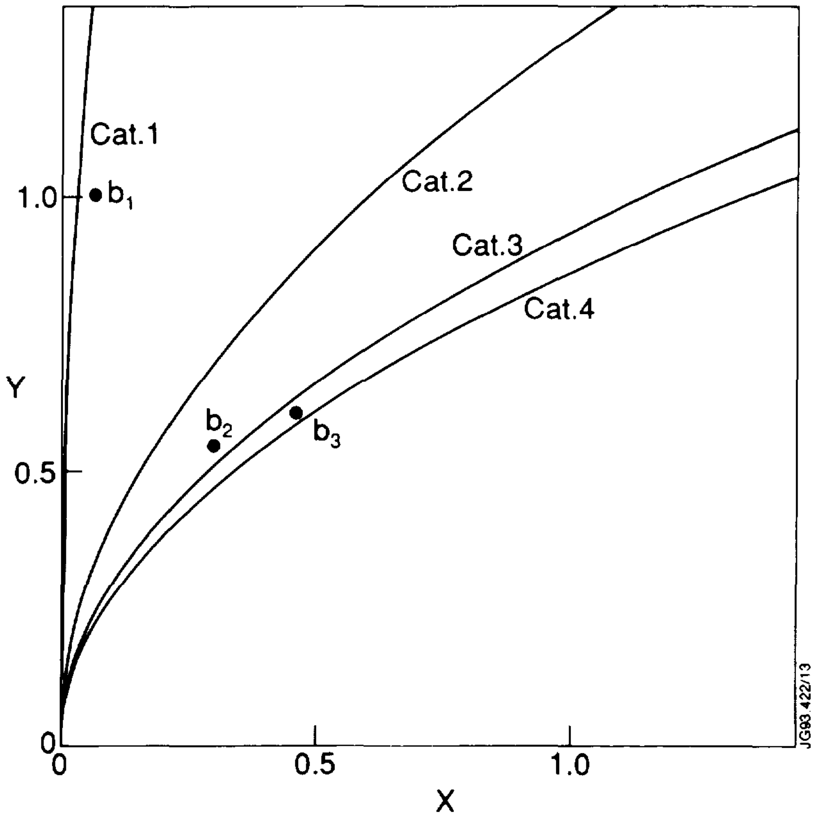

Figure 6: Trajectories in the CMA plane corresponding to the four different categories.

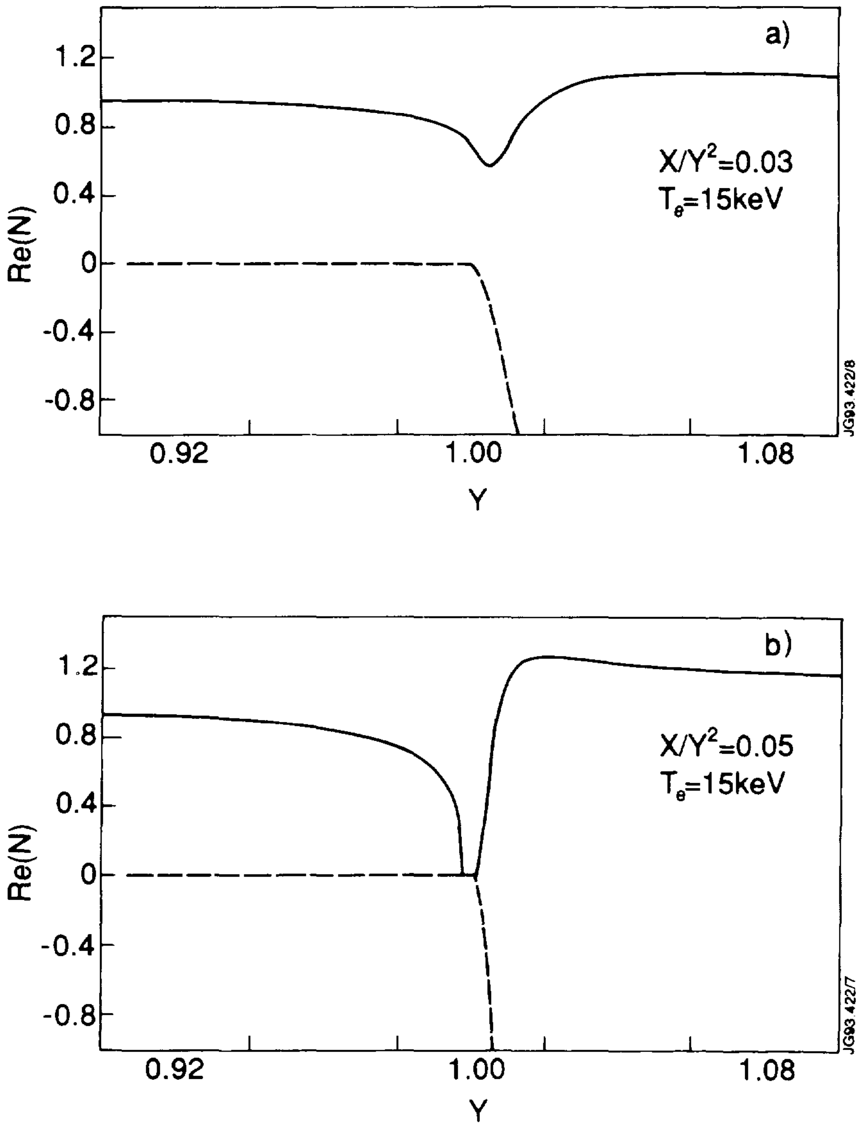

Figure 7: Dispersion curves along a category 1 trajectory as functions of Y with $T_e = 15$ keV and (a) $X/Y^2 = 0.03$, (b) $X/Y^2 = 0.05$.

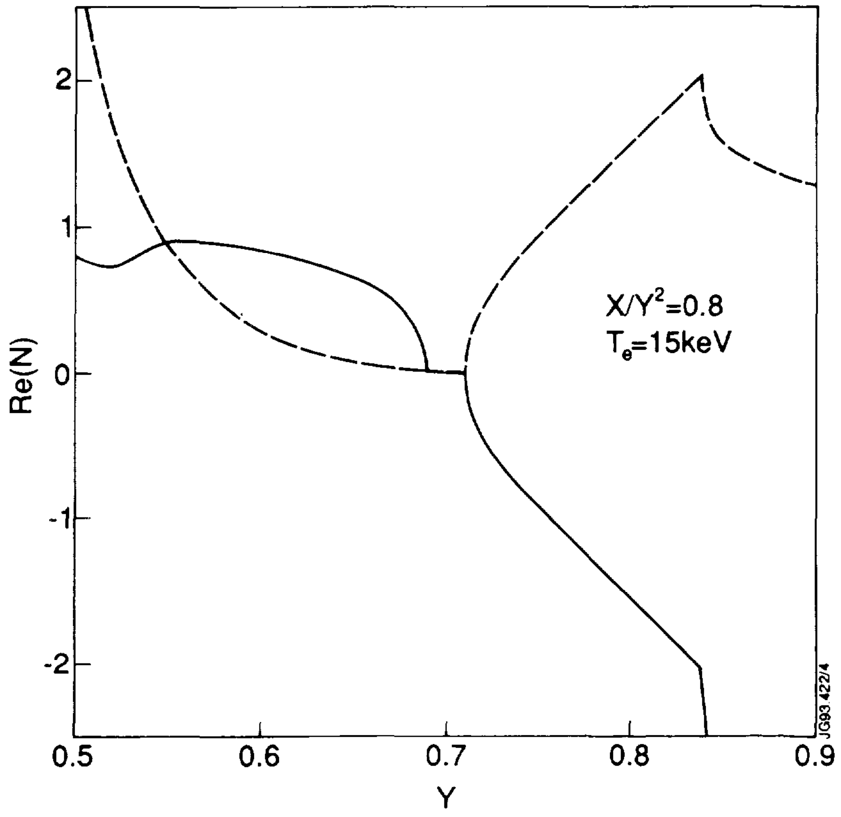

Figure 8: Dispersions curves along a category 2 trajectory as functions of Y with $T_e = 15$ keV and $X/Y^2 = 0.8$.

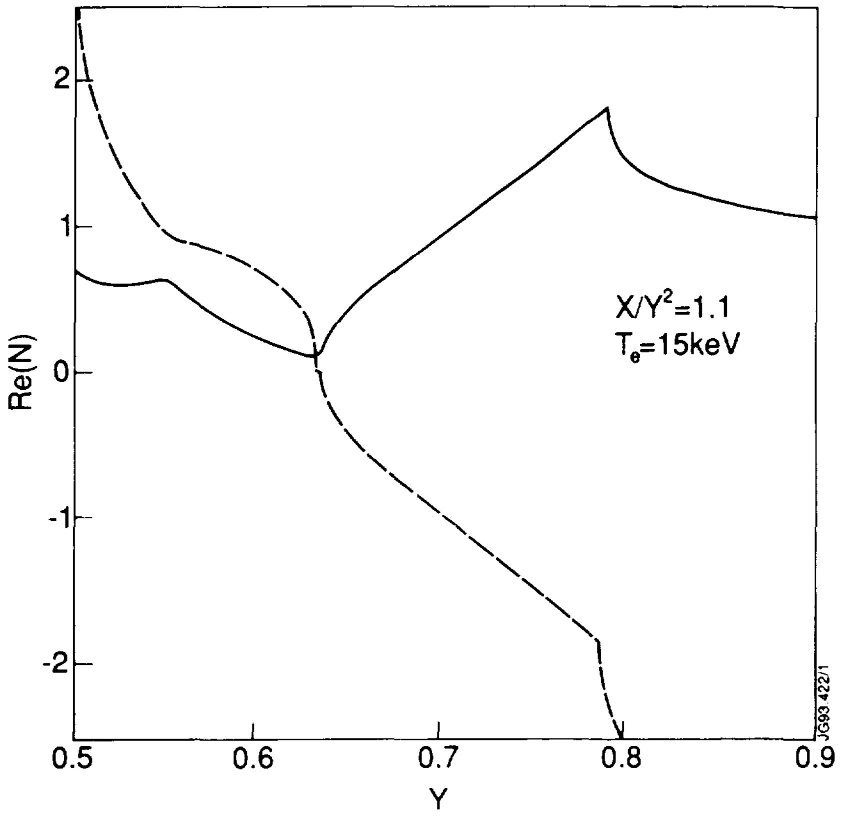

Figure 9: Dispersions curves along a category 3 trajectory as functions of Y with $T_e = 15$ keV and $X/Y^2 = 1.1$.

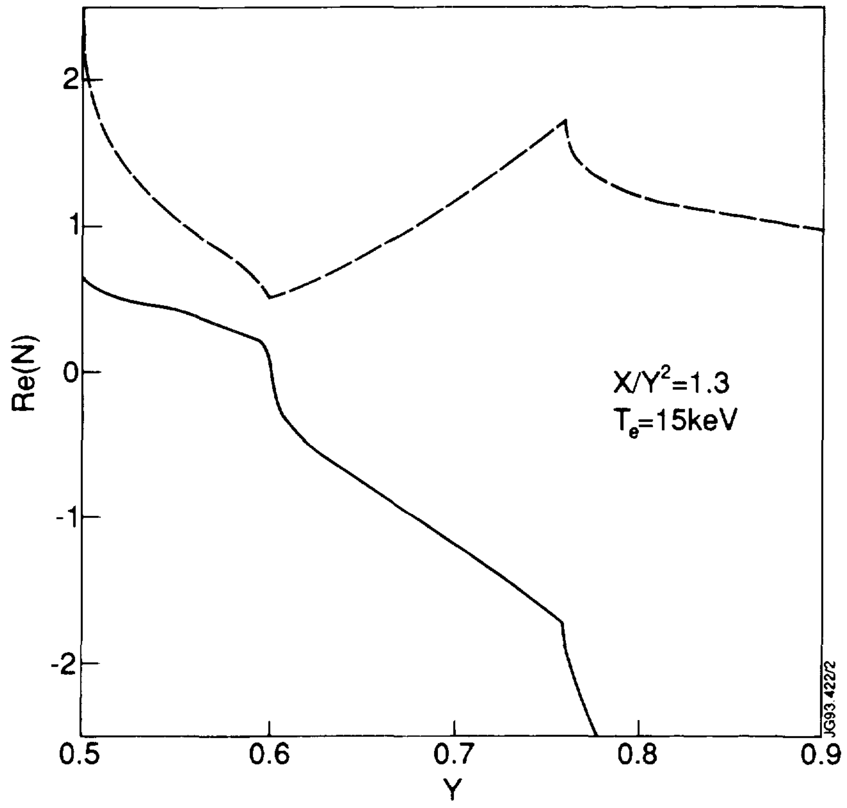

Figure 10: Dispersions curves along a category 4 trajectory as functions of Y with $T_e = 15$ keV and $X/Y^2 = 1.3$.

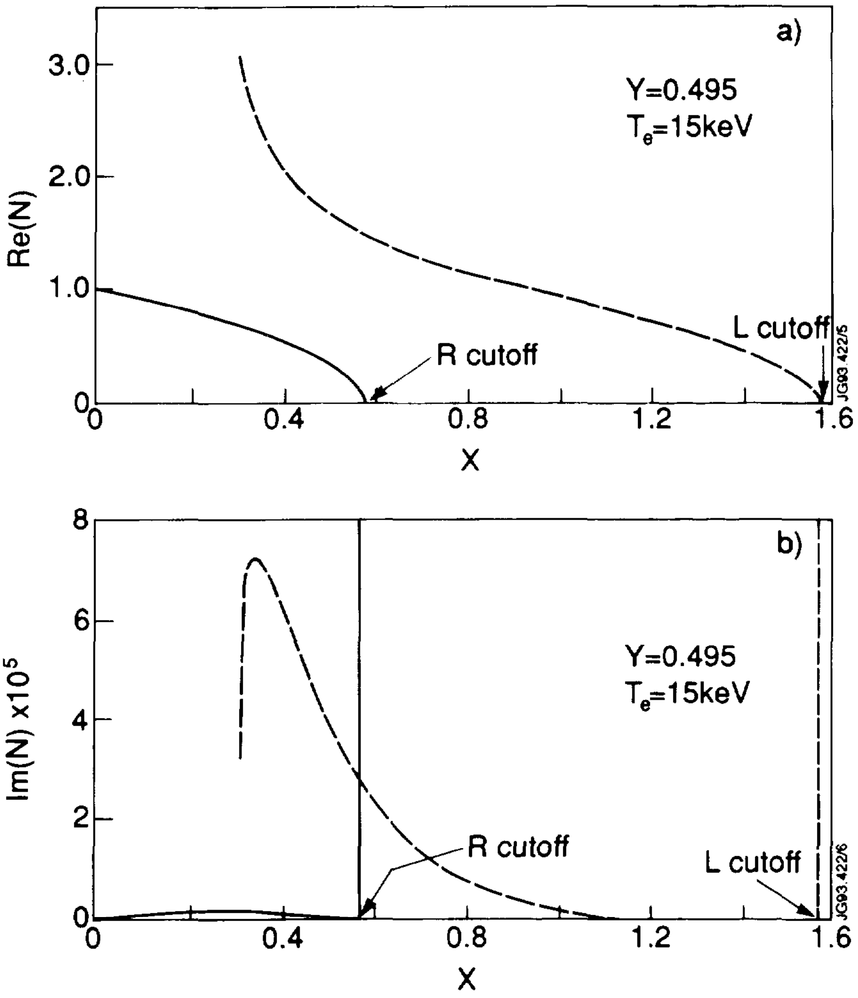

Figure 11: Dispersion of the mode going to the R cutoff (full line) and the mode going to L cutoff (broken line) as functions of X for $Y = 0.495$, T_e=15 keV.

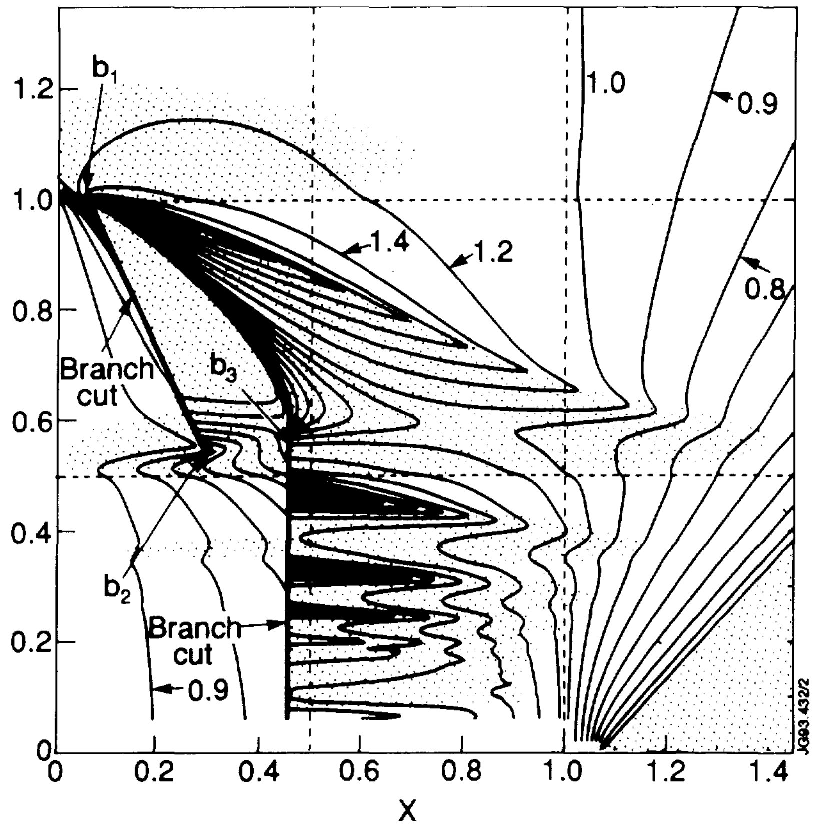

Figure 12: This plot is similar to that in Figure 1, but the branch cuts are placed in different locations.

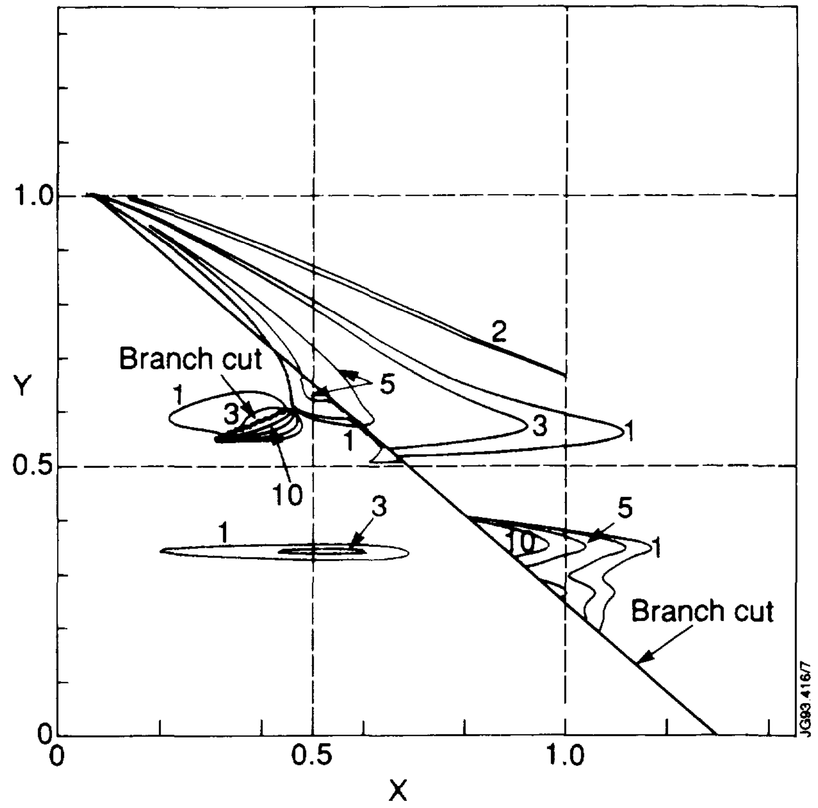

Figure 13: Contour plot of the deviation in per cent between $Re(N_x)$ and $Re(N_{ap})$. Here $Re(N_x)$ is the real part of the weakly relativistic refractive index shown in Figure 1 and N_{ap} is the corresponding solution found with the approximation (4). The plot is obtained with $T_e = 15$ keV and $\theta = 90^0$.

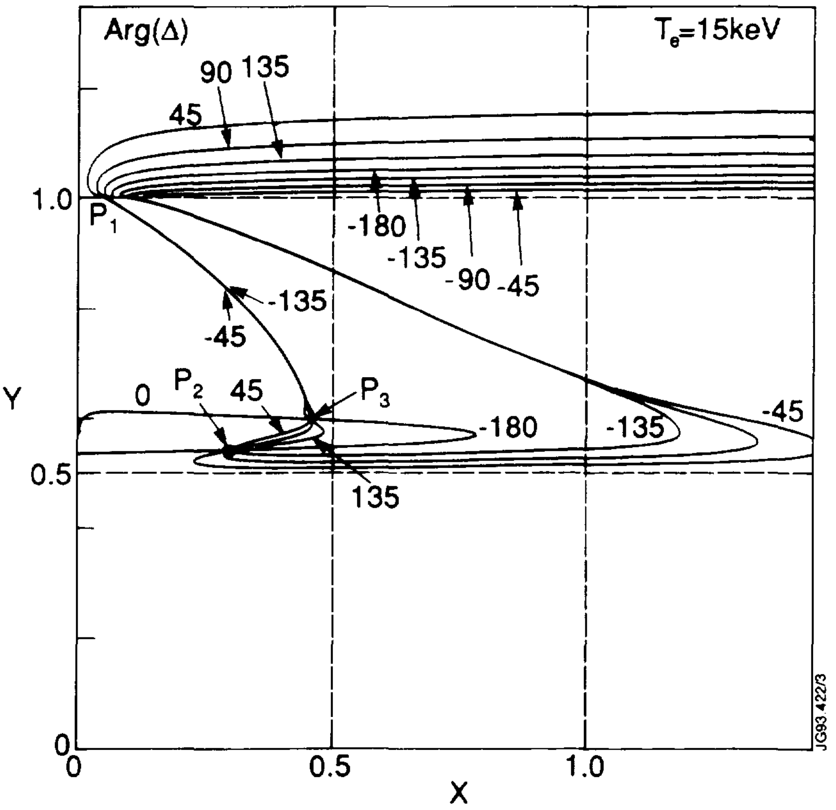

Figure 14: Contour plot of Arg(Δ) in the CMA plane. The steps between the contour levels are 45^0. A specific curve for a level, A, shows the location of the branch cut for the approximation (4) when using a square root with the branch cut placed at the angle A.